Combining X-ray Diffraction and X-ray Absorption Spectroscopy to Unveil Zn Local Environment in Zn-Doped ZrO2Catalysts

(Article begins on next page)

07 August 2024

Combining X-ray Diffraction and X-ray Absorption Spectroscopy to Unveil Zn Local Environment in Zn-doped ZrO$_2$ Catalysts

Davide Salusso[a], Elisa Borfecchia[a]* and Silvia Bordiga[a]

[a] Department of Chemistry, NIS Center and INSTM Reference Center, University of Turin, 10125, Turin, Italy.

*Email: elisa.borfecchia@unito.it

Abstract

Zinc-doped zirconia catalytic properties, promising towards CO$_2$ and CO hydrogenation, are commonly ascribed to the synergic interaction between Zn and Zr. Yet, an atomic-scale perspective on how this synergy is structurally realized remains elusive. In this work, to address this ongoing challenge, we deeply investigated the structure of three Zn-doped ZrO$_2$ catalysts by combining Powder X-Ray Diffraction (PXRD) and X-Ray Absorption Spectroscopy (XAS). PXRD showed the complete formation of a tetragonal solid solution, undistinguishable by Rietveld Refinement from the cubic polymorph. Fit of Extended X-Ray Absorption Fine Structure (EXAFS) spectra at Zr and Zn K-edges unveiled the presence of hexagonal/cubic ZnO nanoclusters embedded and chemically bonded to the tetragonal ZrO$_2$ matrix. Concentration of Zn dopant was evaluated from both PXRD and EXAFS analysis. *In situ* EXAFS study of the catalyst during activation further confirmed the presence of a chemical interaction at ZnO/ZrO$_2$ interface, most probably the active site towards CO$_2$ hydrogenation. ZnO cluster radius was found in the 11-13 Å range, using the Greegor and Lytle spherical model. Taken together, the results demonstrate how the combination of X-ray techniques

probing both long-range and local structural properties could unlock an unprecedent level of understanding in mixed-metal oxide catalysts.

1   Introduction

Zirconium oxide, commonly prepared in the monoclinic (m-), tetragonal (t-) and cubic (c-) polymorphs, is the only metal oxide potentially displaying acid or basic, as well as oxidising or reducing properties at its surface.[1] For this reason it is widely used as a catalyst[1,2] or catalyst support.[3] ZrO_2 surface can be generally described as formed by coordinatively unsaturated (CUS) cationic sites (Lewis acid sites, such as Zr^{4+} and Zr^{3+}), CUS Zr^{4+}-O pairs, oxygen vacancies (V_O) and terminal and multi-coordinated hydroxyls.[4] These wide variety of acid/basic sites makes ZrO_2 a versatile catalyst able to promote many different reactions. Due to the drastic increase of CO_2 anthropogenic emissions,[5] catalytic reactions of major interest involve CO and CO_2.[6] Carbon mono and dioxide are activated on the ZrO_2 surface throughout carbonates formation.[4] Doping with aliovalent cations can tune the surface physicochemical properties, i.e., inducing formation of V_O (Zn^{2+}, Cu^{2+}, Y^{3+})[7,8] neighbouring a CUS Zr^{4+}, which act as strong basic and acid sites, respectively.[9]

Among all the dopants, Zn has been recently investigated for several reactions.[8,10–18] Its ionic radius, comparable to the Zr^{4+} one (0.60 vs 0.84 Å),[19] permits to Zn ions to easily dissolve in the ZrO_2 lattice. The addition of Zn^{2+} likely creates oxygen vacancies, modifying oxygen mobility and tuning the surface physicochemical properties. In the last decade, Zn-doped ZrO_2 (ZZR) has been studied for its properties in CO/CO_2 hydrogenation[13,18,20,21] and ethanol/propene dehydrogenation.[11,12,17] As H_2 can be activated through an heterolytic dissociation on ZnO, the presence of Zn-O pairs or ZnO clusters enhances the hydrogenation/dehydrogenation properties of the catalyst. In the last years, ZZR was also investigated for its catalytic activity and selectivity when used as the oxidic component forming bifunctional catalysts for the direct conversion of CO or CO_2 with H_2 to olefines and

aromatics.[16,18,20,21] Particularly, a balanced Zn:Zr ratio allows to strongly activate CO_2 and CO forming carbonates which are selectively hydrogenated to methanol by H_2 activated over Zn-O.[4,20,21]

However, if much is known about ZZR catalytic properties, detailed information about its structure is still largely lacking. According to DFT calculations, substitution of ZrO_2 units with ZnO induced V_O formation which favoured the simultaneous CO_2 adsorption and H_2 dissociation,[20] suggesting that the catalyst becomes active when Zn maintains a ZnO-like coordination. While in case of Zn-impregnated ZrO_2, its structure was unchanged,[10,12] t-ZrO_2 has been mostly observed in ZZR obtained by coprecipitation,[20–23] showing that the presence of V_O stabilizes the tetragonal polymorph. The effective presence of ZnO-ZrO_2 solid solutions was observed by several laboratory techniques, based on the following lines of evidence: i) the substitution of Zr by Zn causes a shrink of the tetragonal lattice, observable by PXRD from the (101) Bragg reflection systematic shift;[20,21] ii) UV-Vis spectra of ZrO_2 is modified by the dopant, indicating the probable presence of isolated Zn^{2+};[11] iii) FTIR bands around 500 and 600-700 cm^{-1} were associated to the Zn-O-Zn and Zn-O-Zr vibrations.[14] By EXAFS fitting, Han et al.[12] showed that in Zn-impregnated ZrO_2, ZnO aggregates are formed. Nevertheless, when the two oxides are coprecipitated, it is unclear what is the chemical environment surrounding Zn in the ZrO_2 lattice. Due to the indirect effects on the ZrO_2 lattice, Zn^{2+} has been considered as bonded to it, forming a solid solution with the host matrix.[21] However, it is still not clear whether it is present as single isolated Zn sites or as small ZnO_x clusters invisible to PXRD.

We recently investigated CO_2 hydrogenation over the oxidic catalyst for ZrO_2 doped with 5, 15 and 30 wt.% of Zn showing 7, 7.5 and 8% of CO_2 conversion, respectively, at 300°C/15 bar.[20] Even if these performances are lower than those of the conventional Cu-based catalysts,[24] ZZR showed excellent properties when combined with a zeolite/zeotype (SAPO-34 and H-ZSM-5) for the direct conversion of CO_2 to light olefines.[20] We investigated catalytic properties for olefines production in a previous work where we also reported the stability of ZZR/zeolite physical mixture under reaction conditions.[20]

The XAS data, measured during a catalysis-oriented *in situ* experiment, are hereafter critically compared with the complementary results from PXRD and thoroughly analysed to unveil Zr and Zn local structure. ZnO nanoclusters chemically bonded and embedded in the ZrO_2 matrix are unambiguously identified, leading to a consistent structural picture further on validated by Zr and Zn K-edge EXAFS fits performed on the data collected at both room temperature and during the activation protocol, i.e., heating up to 400°C under H_2 flow. ZnO cluster dimension is evaluated using the Greegor and Lytle spherical model,[25] and hypothesis on V_O location and reaction active site are made.

2   Experimental and Theoretical methods

2.1   *Sample preparation*

The three ZrZn-X samples were prepared by colloidal impregnation from Zr and Zn inorganic salts solutions. The -X suffix represents the Zn loading quantified by ICP analysis. The complete synthesis procedure together with detailed elemental analysis results can be found elsewhere.[20]

2.2   *Powder X-ray Diffraction*

All the Powder X-Ray diffraction patterns (PXRD) here reported were measured with a PW3050/60 X'Pert PRO MPD Diffractometer from PANalytical working in Bragg-Brentano geometry, equipped with a Cu $K_{\alpha1,2}$ X-ray source. The three samples were measured in the as-prepared form in transmission mode using a glass capillary (Ø=0.5mm) in the 10-90° 2θ range. The as-prepared ZrZn-5 sample was further measured at room temperature (RT) in reflectance mode with a flat sample holder in the 10-140° 2θ range using ¼'' slits and 0.008 s time/step in order to minimize peaks overlaps. Lattice parameters, phases composition (ZrO_2/ZnO) and peak profile were refined using the Rietveld method implemented in the FullProf software.[26] Thompson-Cox-Hastings approximation[27] was used to describe peak shape following the procedure reported in a previous work.[20]

2.3 X-Ray Absorption Spectroscopy

Zr and Zn K-edges were collected quasi-simultaneously in transmission mode at the Quick-XAS ROCK (Rocking Optics for Chemical Kinetics) Beamline[28] of the French Synchrotron SOLEIL using two quick-XAS monochromators, i.e., Si(111) for Zn K-edge (9659 eV) and Si(220) for Zr K-edge (17998 eV). The two monochromators were mounted on a cam-driven tilt table oscillating periodically around a fixed Bragg angle. Ionization chambers were employed to measure incident (I_0) and transmitted (I_1) beam. Zn and Zr metal foils were measured simultaneously with all the acquired spectra by a third ionization chamber (I_2) in order to achieve a precise energy calibration. Sample thickness was optimized in order to compromise absorption length at both edges. As the measurement was part of a previous catalytic experiment under *in situ* conditions (high pressure/high temperature) the three catalysts were mortar grounded with H-ZSM-5 zeolite and loaded in a quartz capillary reactor (ø=1 mm). The full catalytic experimental procedure was already described in the same work.[20] We hereby report a deeper structural data analysis concerning the XAS spectra measured: i) at RT for the three samples in He atmosphere, ii) under activation, i.e, heating (RT to 400°C, 5°C min^{-1}) at 1 bar in pure H_2 flow, and a qualitative interpretation of spectra collected iii) under reaction conditions, i.e., feed of CO_2 : H_2 : He = 1.25 : 7.5 : 1 (mL min^{-1}) at 300°C and 15 bar pressure. As previously discussed, the presence of the zeolite did not alter the structure of the ZrZn-X phase, so therein it will be safely considered as a spectroscopically-silent spectator. The RT dataset was obtained as the average of 190 scans for an exposure time of 47.5 s and a total time/scan of 95 s while the time-resolved dataset throughout activation and reaction was obtained as average of 50 scans for an exposure time of 12.5 s and a total time/scan of 25 seconds. Energy sampling of 2 eV was used for the two edges and it was intensified in the main edge region to 0.2 eV for Zn (9530-9780 eV) and 0.4 eV for Zr (17971-18120 eV). Pure hexagonal ZnO and tetragonal ZrO_2 powder reference compounds, were measured at the same beamline, in the form of self-supporting pellets. XAS spectra were aligned in energy, background subtracted and normalized to unity edge jump using the Athena

software from the Demeter Package.[29] All the structures and pictorial representation of scattering paths provided in this work were prepared using the Vesta software.[30]

2.3.1   EXAFS analysis details

The $\chi(k)$ EXAFS function and its Fourier transform (FT) were extracted and calculated, respectively, using the Athena software from the Demeter package.[29] EXAFS fitting was performed using the Artemis code within the same package, according to the strategy separately detailed in the following for each investigated absorption edge. EXAFS fitting procedure of RT-spectra was applied to the average of two sequentially measured datasets (each consisting of the average of 190 scans), merged after checking reproducibility among the two acquisitions. For clarity, the original k-space spectra for the three samples are reported in Fig. S1.

2.3.1.1 Zr K-edge at RT under He. Fits were performed in R-space in the $\Delta R = 1.15 - 4.00$ Å range, on the FT of the k^2-weighted $\chi(k)$ EXAFS spectra transformed in the $2.5 - 12.0$ Å^{-1} range. FEEF6[31,32] code implemented in the Artemis software was used to calculate theoretical amplitudes and phases. As input for all the FEFF6 calculation we employed a tetragonal ZrO_2 crystallographic information file (CIF) available in the literature.[33] ZnZr-X lattice parameters were taken from PXRD Rietveld refinement (Table S1).

Zr K-edge EXAFS spectra for the ZrZn-X series were fit considering all the single scattering (SS) paths contributing to the analysed R-space range. A triangular multiple scattering (MS) path between Zr-O(1)-O(2), where O(1) and O(2) are the two oxygens in the Zr first coordination shell (Fig. S4b) was also included. We attributed independent radial shift (ΔR) and Debye Waller factor (σ^2) to O(1), O(2) and Zr while the same energy shift parameter (ΔE) was used to optimize all the scattering paths. To reduce the number of optimized variables and evaluate a physically meaningful Zr-Zr coordination number (CN), we considered chemical transferability to import the amplitude reduction factor as S_0^2 (0.97 ± 0.13) from the optimized EXAFS fit of a reference tetragonal ZrO_2 (see SI, Fig. S5 and Table

S2). As underlined by the Kröger-Vink notation[34] in eq. (1) below, in ZrZn-X the Zr neighbourhood is modified by an oxygen vacancy (V_O) by the dopant Zn_{Zr}.

$$(1 - x)Zr_{Zr}^{x}(x)Zn_{Zr}''(2 - x)O_{O}^{x}(x)V_{O}^{\circ\circ} \qquad (1)$$
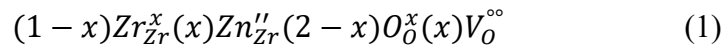
Zn doping was then considered by including an extra Zr-Zn SS path at the same distance of the Zr-Zr one (3.587 Å) and by describing the associated coordination number with an extra variable "*Zn*". This variable was also used to describe Zr nearest neighbour (NN) V_O (i.e., expressing oxygen degeneracy of the first coordination shell as 4-Zn/2 for O(1) and 4-Zn/2 for O(2)) and next nearest neighbour (NNN) Zn (i.e., changing Zr coordination to 12-Zn).

2.3.1.2 Zn K-edge at RT under He. Fits were performed in R-space in the ΔR = 1.0 – 3.3/1.0 - 3.5 Å range, on the FT of the k^2-weighted $\chi(k)$ EXAFS spectra transformed in the 2.5-13.0 $Å^{-1}$ range. FEEF6 code implemented in the Artemis software from the Demeter package was used to calculate amplitudes and phases. As input for FEFF6 calculation we employed standard geometries available in the literature[35,36] and an *ad hoc* Zn-doped tetragonal ZrO_2 CIF file described in the SI (Table S4).

At the Zn K-edge the most informative sample was ZrZn-15. It presented the best balance between Zn loading (best signal-to-noise ratio) and phase purity (absence of segregated bulk ZnO, as described in the following Section 3.1). FT-EXAFS extraction and fitting were therefore conducted only for this sample. S_0^2 (0.86 ± 0.10) optimized for reference h-ZnO (see SI Section 3, Fig. S8 and Table S3) was exported to the fit while different geometries were considered as input structures for theoretical paths calculations: i) t-ZrO_2 ($P4_2nmc$) with the Zr^{4+} substituted by Zn^{2+} (t-$ZnZrO_2$) (Table S4), ii) ZnO in the hexagonal ($P6_3mc$) wurtzite polymorph (h-ZnO)[35], iii) ZnO in the cubic (F4-3m) zinc blende polymorph (b-ZnO),[36] and, iv) in the most advanced fitting model (h-ZnO/ZrO_2), ZnO nanoclusters chemically bonded to the ZrO_2 matrix. Structures and fit procedures are described in the SI Section 5.

2.3.1.3 Cluster size evaluation. Considering the uncertainties intrinsically affecting our XAS measurements (i.e., Debye-Waller (DW) thermal contribution, edge jump optimized for both Zr and Zn edges), ZnO nanocluster shape has been approximated to a sphere. Greegor and Lytle formula, eq. (2),[25] was used to evaluate average nanoparticle dimension from the Zn-Zn coordination number resulting by EXAFS fit.

$$CN\ (R) = \frac{1}{R^3}\Big[(R - R_i)^3 * N_i + \sum_n (3\Delta R_n^2 + 3\Delta^2 R_n + \Delta^3) F N_i\Big] \qquad (2)$$

Where CN is the coordination number, evaluated as a function of the radius R of the particle (assumed to be spherical) by summing unterminated coordination spheres in the inner regions R-R_i with a summation over successive terminated coordination spheres of radius R_K in the outer regions $(R$-$R_i)<R_K\leq R$.

For a more detailed description of eq. (2) and of the related parameters employed in this work, the reader is referred to SI Section 6 (eq. S1).

2.3.1.4 Fit of *in situ* EXAFS data during catalyst activation under H$_2$. During catalyst activation, 100 spectra (each consisting of the average of 50 scans) were collected at Zr and Zn K-edges. EXAFS analysis was carried out on 10 spectra selected at constantly spaced temperatures from 310K to 673K. For clarity, the original k-space spectra are reported in Fig. S2. To find the structure describing the whole temperature evolution, the 10 spectra for the same absorption edge were collectively fit. To reduce the number of fitting variables, DW factors were described with the Einstein model introduced by Sevillano et al.[37] and already applied in literature for describing catalysts during thermal treatments.[38,39] Briefly, the model allows describing a single scattering path with three parameters: i) a fixed temperature factor, defined as the sample experimental temperature, ii) the reduced mass of the absorber-scatterer pair, calculated by IFEFFIT (implemented in the Artemis software) and iii) the Einstein temperature. As the latter one is temperature independent, it does not change between datasets but only among scattering paths, allowing a drastic reduction in the number of fitting variables. High values of Einstein temperature are associated to a lower DW value. For the sake of

clarity, considering the complexity of the Einstein model, and the presence of intrinsic temperature measurements errors, we considered out of the scope of this work the evaluation of the errors affecting the so found DW factors.[40] Since the Einstein model cannot describe a possible structural phase evolution during the analysed spectral series, as hereafter described, we assumed the absence of phase transitions during the *in situ* experiment, as supported by the overall limited variations observed in both XANES and EXAFS regions at both Zr and Zn K-edges.

3   Results and discussion

3.1   *Powder X-ray Diffraction (PXRD)*

As already discussed in a previous work,[20] PXRD diffractograms for the ZrZn-X series, shown in Fig. 1, contain the same Bragg reflections, despite for a series of extra peaks in the ZrZn-30 sample associated to a hexagonal ZnO extra phase. The common Bragg reflections were initially ascribed to both cubic (Fm-3m) and tetragonal (P4$_2$/nmc) ZrO$_2$ polymorphs. The two structures are not simply discernible from their diffractograms, especially in the case of nanosized crystallites, as evidenced by Rietveld refinement (Fig. 1b, Table S1). Indeed, in this case, peak broadening causes a substantial overlap of reflections, e.g. the (110)$_t$ and (002)$_t$ Bragg peaks which occur at 35.18 and 35.28°, respectively, are convoluted in a single peak not distinguishable from the (002)$_c$ potentially occurring at 35.12°.
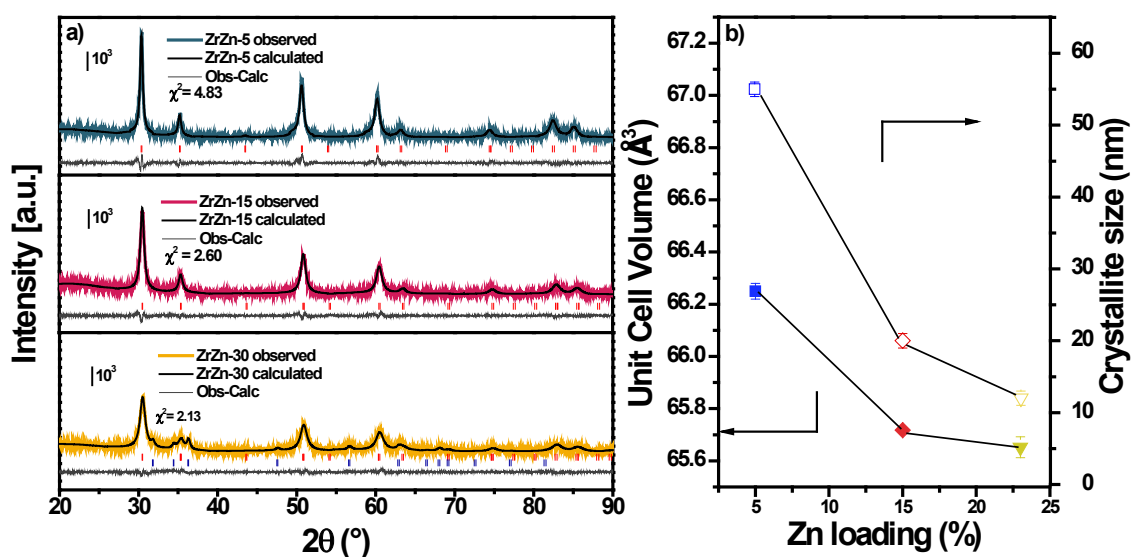
Figure 1. a) PXRD patterns measured for the three ZrZn-X samples in transmission mode using glass capillary sample holder (Ø=0.5mm). Diffractograms for ZrZn-5 (blue curve), ZrZn-15 (red curve) and ZrZn-30 (yellow curve) are reported together with the corresponding refined curves (dark grey) and difference functions (light grey) between observed and calculated curves. t-ZrO2 was used as input structure for the refinement. t-ZrO2 and h-ZnO Bragg reflections are indicated by red and blue vertical sticks, respectively. b) Unit cell volume (full symbols) and crystallite size (empty symbols) obtained from refined lattice parameters and peak shape, respectively, for ZrZn-5 (blue square), ZrZn-15 (red diamond) and ZrZn-30 (yellow triangles).

As showed elsewhere,[20] in the view of the presence of XANES features at the Zr K-edge (Fig. 3) related to the tetragonal ZrO2 polymorph (t-ZrO2), this structure was used to evaluate lattice parameters, phase composition and crystallite size for the three catalysts by Rietveld refinement of PXRD patterns measured in transmission mode (Fig. 1a). h-ZnO (P6₃mc) phase[35] was added to refine the extra reflections in the ZrZn-30 pattern. The obtained results, published in a previous work,[20] are reported in Table S1 for clarity. The effective Zn doping in the ZrO2 structure can be simply verified from the interplanar spacing d_{t-101}/d_{c-111} (where t- and c- stands for tetragonal and cubic, respectively) and the refined lattice parameters. As the Zn^{2+} ionic radius (0.60 Å) is smaller than the Zr^{4+} one (0.84 Å),[19] higher Zn loading consistently translates into a larger shift of the reflection to higher 2θ value

10

(Fig. S3) and a smaller unit cell volume (Fig. 1b). The amount of Zn effectively doping ZrO_2 lattice, also reported in Table S1, was obtained combining Zn wt% from ICP (dopant and segregated) with ZnO wt% (segregated) refined with Rietveld method.

In this work we focused on the laboratory PXRD strengths/limits when investigating cubic/tetragonal ZrO_2 polymorphs, in combination with the Zn influence on lattice parameters. As it presented the most intense/less broadened peaks, ZrZn-5 diffractogram was remeasured in reflection mode to avoid self-absorption phenomena and to enhance the detectability of weak reflections (Fig. 2). Both cubic (Fm-3m)[41] and tetragonal (P4$_2$/nmc)[33] ZrO_2 were used as input geometries to refine the pattern by Rietveld method. Starting values for the lattice parameters were simply calculated from the $(002)_{t/c}$ and $(200)_t$ Bragg reflections at 34° and 50° respectively. Refined curve in Fig. 2 shows a good data/fit agreement factor for both the input geometries. Nevertheless, the diffractogram displays a weak peak at 43° (Fig. 2 inset), which is not expected in the cubic structure whilst it is indexed as (102) using the tetragonal polymorph. Nevertheless, the aforementioned fingerprint is intrinsically weak and close to the noise level. A more careful analysis of the XAS data previously reported was necessary to complementary solve the catalyst structure.
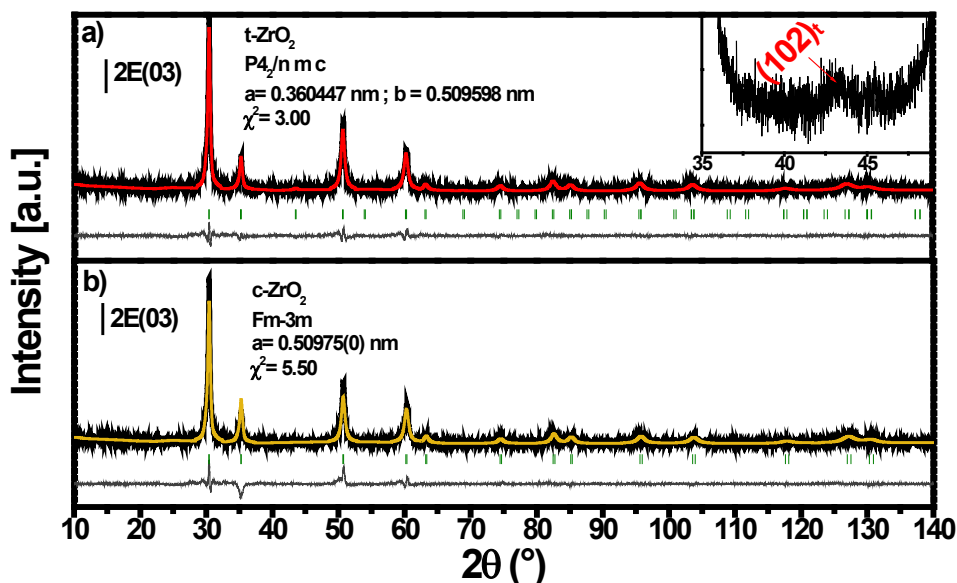
Figure 2. PXRD pattern of ZrZn-5 measured in reflection mode using a glass flat holder collected in the 10-140° 2θ range. Experimental data (dark curve) and calculated curve for a) tetragonal (red curve) and b) cubic (yellow curve) structures are compared. Difference function between observed and calculated curves is reported below each diffractogram (thin grey curve). Tetragonal (102) reflection is showed in the inset. t-ZrO_2 and c-ZrO_2 Bragg reflections are indicated by green vertical sticks.

3.2 *X-ray Absorption spectroscopy (XAS)*

3.2.1 Zr K edge XAS

3.2.1.1 XANES. XAS spectra of the three samples measured at RT in He atmosphere are reported in Fig. 3, together with those of monoclinic and tetragonal ZrO_2 polymorphs, as references. Edge position, giving important information on the absorber atom oxidation state, is observed at energy typical of Zr^{4+} for all the samples. White-line peak is split into B and B' features while multiple-scattering feature C occurs in the post-edge region. These two latter fingerprints allow to safely distinguish between tetragonal and monoclinic polymorphs, confirming PXRD results. Moreover, based on previous literature reports,[42,43] it is possible to distinguish tetragonal/cubic polymorphs from the presence/absence of a pre-edge shoulder (labelled as 'A' in Fig. 3), more visible considering the

12

XANES first derivative (Fig. 3, bottom inset). This feature was initially attributed from electron-energy loss spectroscopy,[42] and subsequently confirmed from the Zr K-edge XANES studies by Li et al.[43] to stem from a 1s→4d transition, characteristic of t-ZrO_2. In the latter polymorph Zr coordination changes from ZrO_7 centrosymmetric unit, typical of pyrochlore-like structures (i.e., c-ZrO_2), to a distorted ZrO_8 one. To incorporate the extra oxygen, Zr-O forms two non-equivalent tetrahedra, where four oxygens are closer (O(1)) to the Zr atom and four are farther (O(2)) (Fig. S4a). As showed in the inset in Fig. 3, the pre-edge peak is observed for all the ZrZn-X catalysts, confirming, throughout the series of samples, the tetragonality of the ZrO_2 matrix. Notably, these indications from Zr K-edge XANES corroborate those from PXRD, with respect to the weak (102) reflection observed in the higher-quality pattern of ZrZn-5 (Fig. 2, inset).

The main edge width in the Zr K-edge (Fig. 3, top inset) spectra could be also indirectly associated to the presence of Zn as Zr NNN, as confirmed later on by Zr and Zn K-edge EXAFS fit (Sections 3.2.1.2 and 3.2.2.2). The main edge width, also described as the FWHM of the first derivative main peak (Fig. 3, bottom inset), is an indicator of the absorber symmetry. In particular, a higher coordination symmetry is expected to reflect into a smaller first derivative main peak FWHM. In Fig. 3 inset and Fig. S6 (SI, Section 2) we observed a FWHM increase at higher Zn loading, showing that the presence of Zn distorts Zr NNN environment.
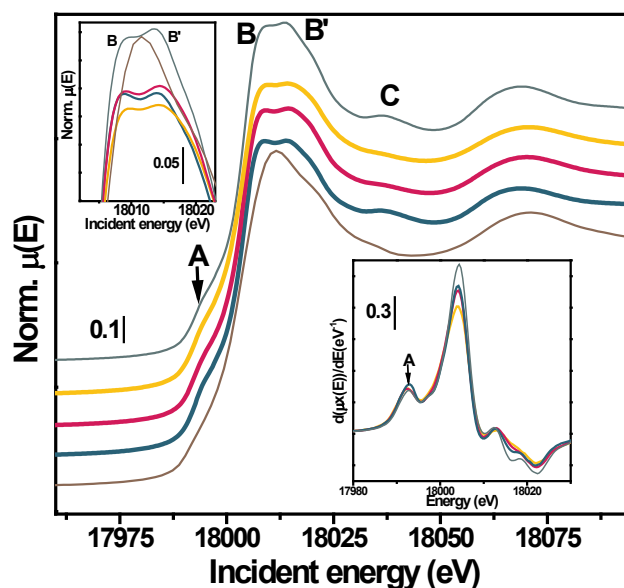
Figure 3. Stacked representation of Zr K-edge XANES measured at RT (He atmosphere) for the three ZrZn-X samples. ZrZn-5 (blue), ZrZn-15 (yellow) and ZrZn-30 (red) are represented together with reference tetragonal (grey) and monoclinic (brown) ZrO_2 polymorphs. Top left inset: non-stacked detail of the white-line peak. Bottom right inset: XANES first derivative enhancing the pre-edge feature related to the 1s→4d transition.

3.2.1.2 EXAFS. Phase-uncorrected Zr K-edge FT-EXAFS are reported in Fig. 4a,b. Similar features for the spectra of the three ZrZn-X catalysts are observed. The two main peaks located at 1.5 Å and 3.2 Å can be safely connected to the NN Zr-O and NNN Zr-Zr SS contributions. As already reported,[44] at RT the Zr-O peak sub-shell structure characteristic of t-ZrO_2 is not evident from qualitative observation of the EXAFS data. The first-shell peak intensity is comparable between all the samples and substantially equivalent to that observed for the t-ZrO_2 model compound. Conversely, the second-shell peak displays a lower intensity than that observed for the reference t-ZrO_2, unveiling an enhanced structural disorder in the Zr local coordination environment. Most importantly, the peak intensity is progressively abated as Zn doping increases (Fig. 4a). A comparison of the imaginary parts of the Zr-Zr and Zr-Zn scattering contributions (Fig. 4c) extracted after EXAFS fitting in the

representative case of ZrZn-30 (vide infra) shows that they cancel each other out perfectly, linking the chemical Zn doping in the ZrO₂ structure with the intensity observed decrease of the second-shell peak in Zr K-edge EXAFS.
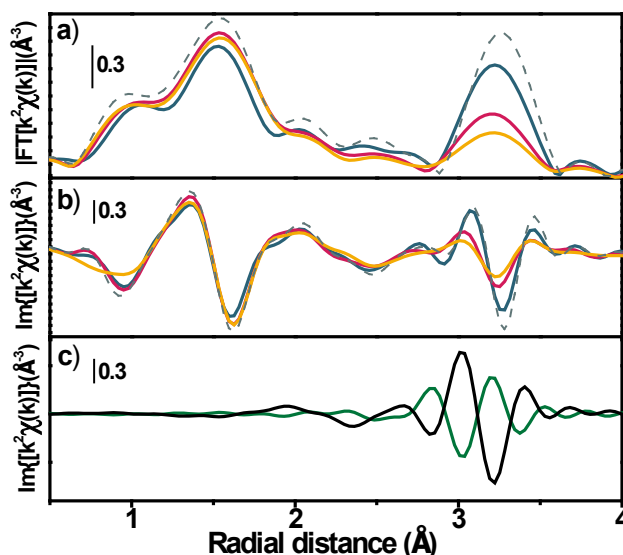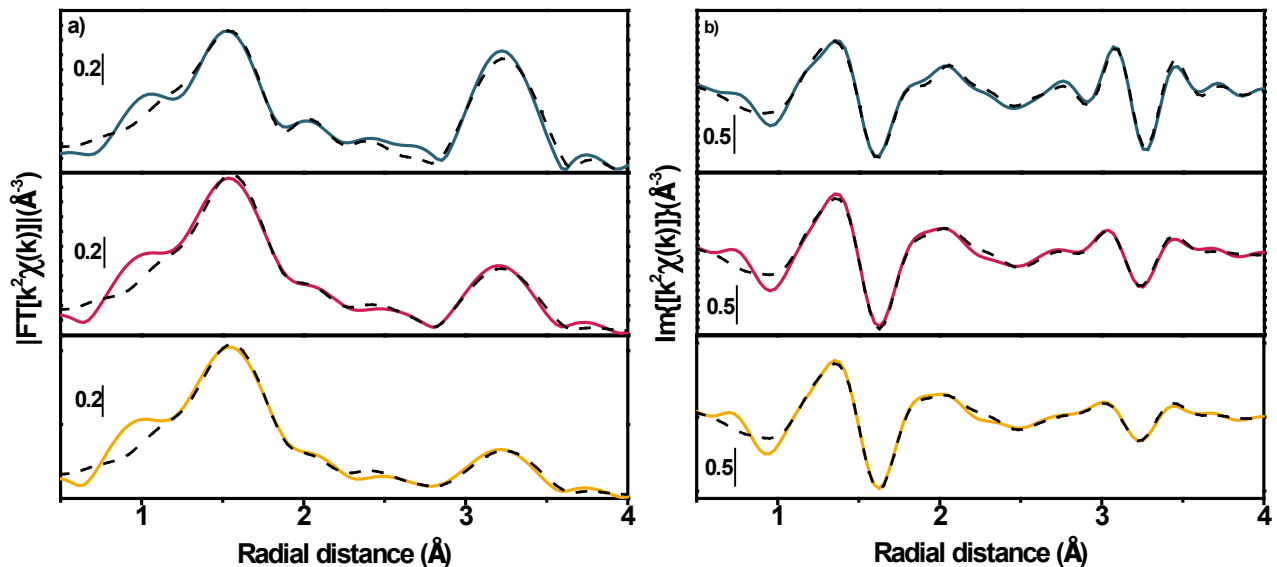

Figure 4. a) Magnitude and b) imaginary parts of k^2-weighted phase-uncorrected FT-EXAFS extracted in the k-range 2.5-12.0 Å^{-1} for ZrZn-5 (blue), ZrZn-15 (red), ZrZn-30 (yellow) and reference t-ZrO₂ (dashed grey). c) Imaginary part of the individual Zr-Zr (black) and Zr-Zn (green) scattering paths generated by FEFF6 optimized after the fit of ZrZn-30.

EXAFS fits started from a tetragonal ZrO₂ model, used as initial geometry input for the refinement. The whole procedure, described in detail in Section 2.3.1.1 and in the SI, Section 2, led to the best-fit curves reported in Fig. 5. A good agreement was observed for both magnitude and imaginary part of the FT-EXAFS spectra when comparing experimental and calculated curves. Physically meaningful values for energy shifts, radial shifts and DW factors (σ^2) were found in all cases. Notably, a higher σ^2 value for NN O(2) was observed in all the samples, as well as in the reference t-ZrO₂ (Table S2). This result, already documented in previous literature for t-ZrO₂,[43,44] is ascribable to the farther spatial position of this oxygen from the Zr absorber. In fact, even if O(1) and O(2) positions are crystallographically equivalent and indistinguishable from PXRD, the Zr-O(2) distance is higher (2.37 Å vs 2.06 Å of Zr-O(1))[33] lowering the bond strength and thus leading to a slight increase in

15

the corresponding σ^2 value.[43] Zr-Zr and Zr-Zn SS paths starting with the same distance were considered for second-shell fitting. It is worth noting the higher value for the Zn σ^2 factor in ZrZn-5, in line with the low Zn concentration in this sample, complicating the optimization of the Zr-Zn scattering contribution in the corresponding EXAFS spectrum. The contribution of each path was modulated by refining Zr coordination number (CN) with NNN Zr/Zn using the 'Zn' variable as described above. Even if EXAFS CNs have a limited accuracy ($\approx$20%), the obtained EXAFS results yielded amounts of Zn chemically doping zirconia in substantial agreement with those obtained by combining elemental analysis and complementary insights from PXRD (Table 1). Yet, a general underestimation of Zn-loading is observed, which will be rationalized in the following (Section 3.2.3), in the view of EXAFS analysis at Zn K-edge.

The Zr-O(1)/O(2) bond lengths are ca. 2.10 Å and 2.24-2.28 Å, respectively, with each sub-shell including $4 - (Zn/2)$ O atomic neighbours. Considering that the obtained values for Zr-O(1) and Zr-O(2) significantly differ within their fitting errors, we can consider the distances information obtained by EXAFS as reliable.

Figure 5. Experimental (coloured lines) and best fit (dashed grey lines) a) magnitude and b) imaginary parts of the k^2-weighted, phase-uncorrected FT-EXAFS spectra for ZrZn-5 (blue), ZrZn-15 (red) and ZrZn-30 (yellow).

Table 1. Results from EXAFS fit of the ZrZn-X samples using tetragonal (t-ZrZn-X) and cubic (c-ZrZn-5) structures as input geometries. Fit was performed in R-space, in the range 1.15-4.00 Å, on FT-EXAFS spectra transformed in the 2.5-12 Å^{-1} k-range, resulting in a number of independent parameters $\pi\Delta R\Delta k/2 > 16$. Amplitude reduction factor ($S_0^2 = 0.97 \pm 0.13$) imported from reference t-ZrO$_2$ was fixed in all cases. R-factor, number of parameters, Zn-O/Zr/Zn radial distance are reported. Zr-O radial distance and σ^2 contains two values for t-ZrZn-X and a single one for c-ZrZn5 as in the cubic polymorph Zr is surrounded by eight equidistant oxygens while in the tetragonal one four oxygen are closer, O(1), and four farther, O(2). The optimized average number of Zn atoms occurring as Zr NNN is reported though the 'Zn' parameter, while related Zn weight percentage for each ZrZn-X catalyst is calculated from this value.

Sample	t-ZrZn5	t-ZrZn15	t-ZrZn30	c-ZrZn5
Fit R-factor	0.017	0.013	0.0086	0.035
Npar (Nind)	10(16)	10(16)	10(16)	8(16)
ΔE(eV)	-3.3 ± 1.3	-2.9 ± 1.2	-3.4 ± 1.1	-5.8 ± 1.5
R$_{Zr-O}$ (Å)	2.100 ± 0.011 2.28 ± 0.03	2.100 ± 0.014 2.25 ± 0.02	2.094 ± 0.013 2.240 ± 0.019	2.133 ± 0.015
σ^2_O (Å^2)	0.004 ± 0.002 0.011 ± 0.005	0.0023 ± 0.0017 0.006 ± 0.003	0.0023 ± 0.0015 0.005 ± 0.003	0.009 ± 0.002
R$_{Zr-Zr}$ (Å)	3.62 ± 0.02	3.61 ± 0.02	3.60 ± 0.03	3.62 ± 0.03
σ^2_{Zr} (Å^2)	0.008 ± 0.003	0.007 ± 0.004	0.010 ± 0.004	0.004 ± 0.003
R$_{Zr-Zn}$ (Å)	3.56 ± 0.10	3.58 ± 0.03	3.57 ± 0.04	3.58 ± 0.04
σ^2_{Zn} (Å^2)	0.0017 ± 0.0019	0.003 ± 0.003	0.005 ± 0.004	-0.0007 ± 0.004
Zn	1.9 ± 1.1	2.6 ± 0.6	3.0 ± 0.5	2.5 ± 0.7
Zn-loading (wt.%) EXAFS	8 ± 9	12 ± 5	15 ± 4	

Zn loading (wt.%) ICP/PXRD	5	15	30 (22)	-

We also attempted a test fit of the ZrZn-5 EXAFS spectrum using as starting input the c-ZrO_2 model. Even if the calculated curve satisfactorily matched the experimental one (Fig. S9), fit results also reported in Table 1 (last column) show a substantially higher R-factor and a negative value for σ^2_{Zn}, making the fit unphysical. Additionally, from a structural point of view we can observe that the Zr-Zr distance resulted from this test fit is significantly elongated with respect to the starting input value, underlying that the cubic structure is distorted to approach the tetragonal one. In fact, in stabilized cubic ZrO_2, Zr-Zr distance evaluated by EXAFS was reported by Li et al. [43] to be ca. 3.55 Å, while 3.62 Å is a value more usual for t-ZrO_2.

3.2.2 Zn K-edge

3.2.2.1 XANES. In order to deeply understand the local coordination and structure of Zn atoms doping the ZrO_2 lattice, we initially focused on the XANES region of Zn K-edge XAS spectra, measured quasi-simultaneously with the Zr K-edge ones. The spectra of the three ZrZn-X samples are reported in Fig. 6, together with Zn K-edge XANES spectra of h-ZnO and Zn metal foil references. The edge position, reflecting the oxidation state of the absorber, highlights the presence of Zn^{2+} in all the samples. Typical h-ZnO spectral features, such as main absorption peak B and post-edge resonance C, are recognized in the XANES spectra of all the ZrZn-X samples. However, shoulder-like features (A, D, E in Fig. 6) present in h-ZnO are substantially dampened in the ZrZn-X catalysts, pointing out a higher defectivity. While for ZrZn-30 the presence of bulk h-ZnO was observed by PXRD (Fig. 1a), in the case of ZrZn-5/15 we cannot specifically connect the ZnO phase to wurtzite or zinc blende, since their XANES spectra are very similar to each other.[45]
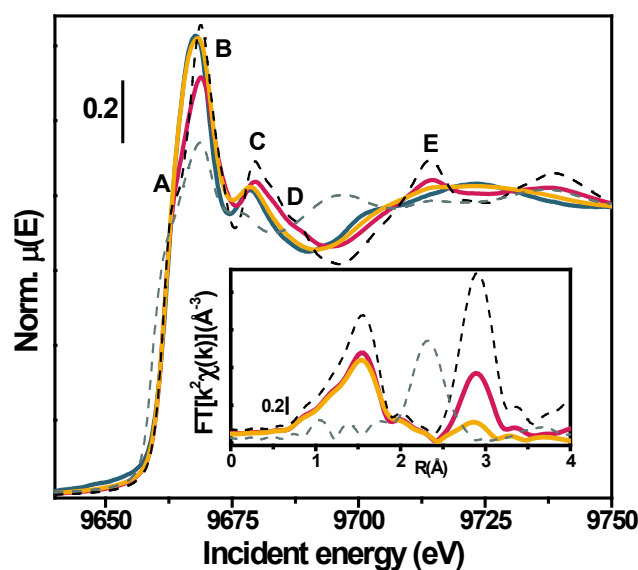
Figure 6. Zn K-edge XANES (main panel) and phase-uncorrected k^2-weighted FT-EXAFS (inset) transformed in the 2-12 Å^{-1} k-range measured at RT (He atmosphere) for the three ZrZn-X samples. Spectra of ZrZn-5 (blue), ZrZn-15 (yellow) and ZrZn-30 (red) are shown together with those of reference h-ZnO (dashed-black) and Zn metal foil (dashed-grey). FT-EXAFS of ZrZn-5 is missing due to the low absorber concentration as observable from Fig. S1b.

3.2.2.2 EXAFS. Detailed information on Zn local environment can be retrieved by a careful analysis of the EXAFS region. As mentioned above, within the limitations dictated by quasi-simultaneous data collection at Zr and Zn K-edges, analysable FT-EXAFS spectra were obtained for the ZrZn-15/30 samples (Fig. 6, inset). In the specific case of ZrZn-30, the contribution from segregated bulk ZnO, highlighted by PXRD (Fig. 1), cannot be easily excluded. Noteworthy, as reported in the introduction, the catalytic properties of the three samples are not drastically different.[20] Hence, considering k-space data quality (Fig. S1b) and absence of segregated phases, for quantitative EXAFS refinement we focused on the ZrZn-15 sample in order to selectively access information on Zn atoms effectively doping the ZrO_2 matrix.

As observed in the Zr K-edge FT-EXAFS (Fig. 4,5), the unit cell volume decrease (Fig. 1b), and the (101) Bragg peak shift (Fig. S3), Zn^{2+} effectively dopes ZrO_2 while locally maintaining a ZnO-like geometry. In order to describe Zn local coordination environment, two main scenarios have to be

considered: i) Zn^{2+} substitutes Zr^{4+} located in position (¼ ¾ ¼) in t-ZrO₂ (P4₂nmc) adapting its interatomic distances to the host lattice, thus forming an ideal t-ZnZrO₂ solid solution (Fig. 7a) and ii) Zn^{2+} does not adapt its interatomic distances and forms a ZnO cluster embedded and chemically bonded to the t-ZrO₂ matrix (Fig. 7b,c).
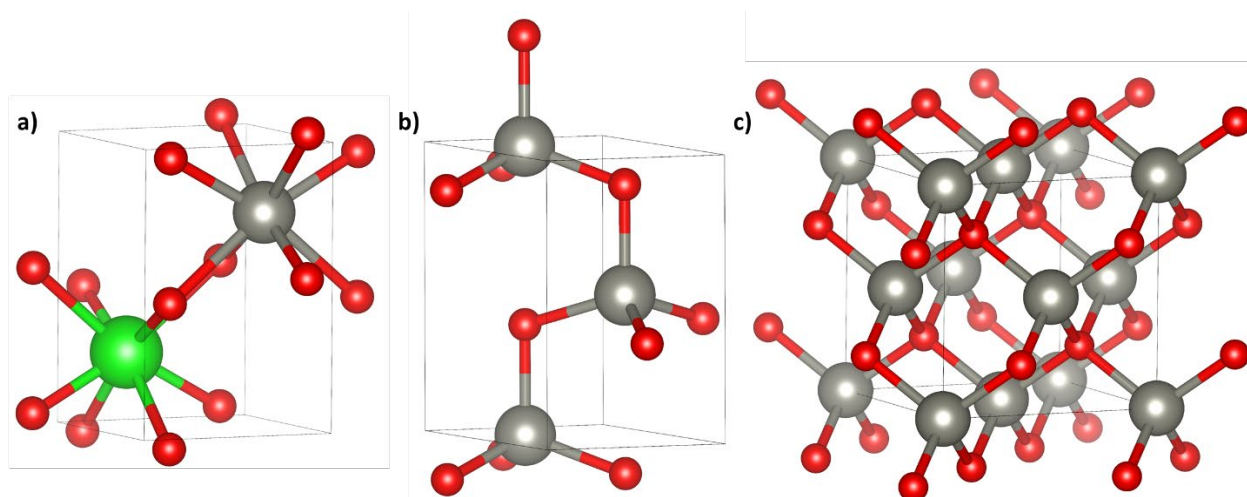

Figure 7. Structures used as input geometries in Zn K-edge EXAFS fits for ZrZn-15. Unit cell of a) tetragonal ZrO₂ (space group P4₂nmc; lattice parameters a = 3.60 Å and c = 5.10 Å[33] from Table S1) substituted with Zn; b) h-ZnO (P6₃mc; a = 3.25 Å and c = 5.21 Å[35]) and c) c-ZnO (F-43m, a = 4.63 Å[36]). Zinc (grey), Zirconium (green) and Oxygen (red) atoms are represented by coloured spheres. Oxygen partial occupancy in model a) is represented by non-filled colours.

The first case seems unreasonable as, to enter in the t-ZrO₂ lattice, Zn should dramatically enlarge its interatomic distance (R_{Zn-Zn}=3.20 Å and R_{Zr-Zr}=3.59Å). From qualitative analysis of the relevant FT-EXAFS spectra, we note that Zn-Zr interatomic distance does not reflect the value obtained from the Zr K-edge fit ($R_{Zr-Zn} \approx 3.5$ Å). Indeed, the Zn-K edge phase-uncorrected EXAFS second-shell peak position (Fig. 6, inset) occurs 0.3 Å below the one at the Zr K-edge (Fig. 5). Furthermore, an EXAFS fit performed using the t-ZnZrO₂ structure to reproduce the EXAFS of ZrZn-15 (Table S5) led to meaningless results, including excessively high radial shifts and a negative σ^2_{Zn} value. Taken together, these lines of evidence allowed us to safely rule out the ideal solid solution scenario.

In the second case we should assume that the cluster dimension consists of only few ZnO unit cells, smaller than the PXRD detection limit. We initially described the cluster structure using i) hexagonal (wurtzite) ZnO ($P6_3mc$), h-ZnO and ii) cubic (zinc blende) ZnO (F-43m), c-ZnO, where in both cases Zn maintains ZnO_4 tetrahedral coordination (Fig. 7b,c).

EXAFS fit in this case yielded physically meaningful results (Fig. S11, Table S5). While the oxygen tetrahedra in the first shell of the two structures are very similar (h-R_{Zn-O} = 1.99 Å and c-R_{Zn-O}= 2.00 Å), the main difference arises from the scattering contributions in the second shell. Indeed, in h-ZnO the 12 NNN Zn are located at two different distances (h-$R_{Zn-Zn(1)}$ = 3.20 Å and h-$R_{Zn-Zn(2)}$ = 3.24 Å), while they are equidistant in c-ZnO (c-R_{Zn-Zn}=3.27 Å), see also Fig. S7 and Table S3 in the SI. Anyhow, based on previous reports,[46] in case of nanostructured h-ZnO only one Zn-Zn SS path with CN = 12 could be safely considered. Fit results in Fig. S11 and Table S5 show an almost identical fitting quality using both the h- and c-ZnO structures. Best-fit σ^2_{Zn} values are acceptable, yet rather high, in both cases. This is not surprising considering the inherently disordered nature of the proposed ZnO nanoclusters chemically bonded in the ZrO_2 matrix. Zn-Zn CN was refined to 4 ± 3, a value far from the ideal bulk condition, corresponding to CN = 12, consistently with the surface-to-bulk ratio increase in nanosized clusters. As previously reported, presence of ZnO nanoparticles on the surface of the ZrZn-X samples investigated here, as well as in other works adopting equivalent synthesis methods, was not observed neither from Raman spectra nor from STEM-EDX analysis.[20,47] We then considered the ZnO clusters as embedded in the ZrO_2 matrix with only part of the surface potentially exposed. Dimensions of ZnO clusters with a given shape can be estimated based on Zn-Zn CNs measured by EXAFS. According to Agostini et al.,[48] only by extending the EXAFS fit at least to the third coordination shell we could obtain a reliable three-dimensional information. In our case, within the available data quality, typical of a catalysis-oriented *in situ* experiment, we preferred to limit the EXAFS fit to the second-shell region. Thus, for the following analysis, we approximated the cluster shape to a sphere. As reported in several previous works,[48–51] under this plausible assumption for the cluster shape, EXAFS CN is univocally correlated to the cluster size. As illustrated in Fig. 8, using

the Greegor and Lytle[25] equation, eq. (2), we determined an average cluster radius of 13 ± 7 Å for the ZrZn-15 catalyst, consistent with a PXRD-silent nanosized phase.
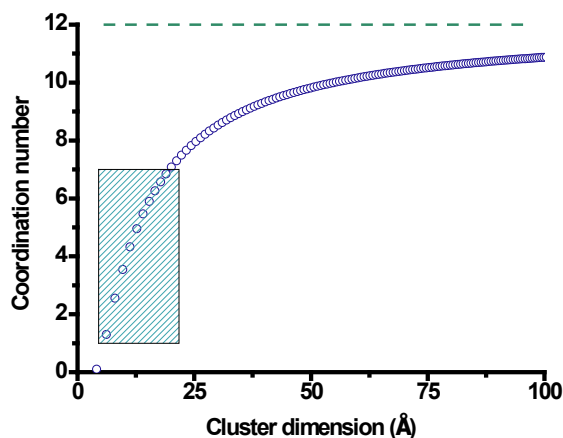

Figure 8. Relation between coordination number and cluster radius evaluated using the Greegor and Lytle equation within the spherical approximation (SI, Section 6). Zn-Zn distance found by EXAFS fit was used as shortest atomic distance. The box indicates the area where our experimental data are located (CN = 4 ± 3). Dashed line indicates the coordination number bulk limit (12).

As observed in Fig. S11, even if h-ZnO gave the best fit for the experimental spectra, it does not fully describe the scattering features located in the 3-3.4 Å range in the phase-uncorrected FT-EXAFS spectrum. Having assessed the presence of h-ZnO clusters embedded in a ZrO_2 matrix, a more careful fit of Zn K-edge EXAFS spectra implies to consider the interface between ZnO cluster and ZrO_2 matrix. Since the Zr-Zn scattering path was consistently observed from the Zr K-edge EXAFS fit (section 3.2.1.2), it is straightforward to consider the presence of this path also in the Zn EXAFS fit. As pictorially represented in Fig. S10 (h-ZnO/ZrO_2 model), we then described the Zn K-edge second-shell region considering one contribution at shorter distance from i) a Zn scatterer located in the ZnO cluster core (Zn-Zn_I) and two contributions at longer distance from ii) a Zn scatterer on the surface of the cluster and chemically connected to Zr (Zn-Zn_{II}), and iii) a Zr scatterer (Zn-Zr). As showed in

Figure 9 and Table S7, considering these two paths globally improved the fit quality, while the relevant fit variables are comparable with those previously obtained using the simpler h-ZnO model. h-ZnO cluster dimension was again evaluated from Zn-Zn$_I$ CN (Table S7), resulting in 11 ± 5 Å, which is in line with the 13 ± 7 Å value priorly obtained (Table S5). At the same time the so obtained radial distances, coordination numbers and DW factors have physically reliable values i.e., Zn-Zr and Zn-Zn$_{II}$ paths are longer than the Zn-Zn$_I$ one, confirming the presence of a h-ZnO/ZrO$_2$ interface, which catalytic role will be discussed in the following sections.
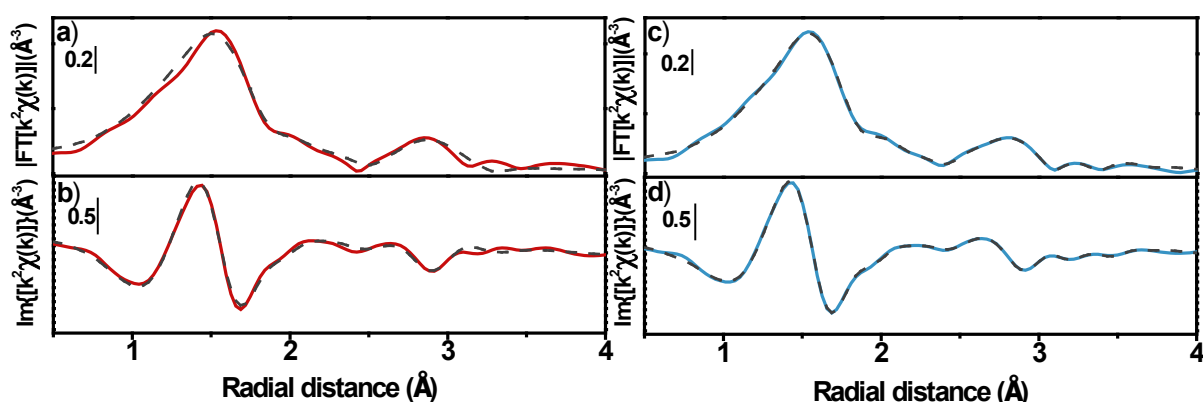
Figure 9. Experimental (solid coloured line) and best fit (dashed grey line) a, c) magnitude and b, d) imaginary parts for k^2-weighted FT-EXAFS of ZrZn-15 using a, b) h-ZnO and c, d) h-ZnO/ZrO$_2$ (Fig. S10) as input structure.

3.2.3   *In situ* EXAFS during activation in H$_2$

Zr and Zn K-edge EXAFS analysis of data obtained at RT in He enabled a thorough description of the as prepared catalyst. Yet, in a catalysis-oriented perspective, it would be of paramount interest also understanding the material structure right before the reaction i.e., after an activation treatment at high temperature under H$_2$. As aforementioned, the ZrZn-15 catalyst showed the best compromise between signal quality (Fig. S1b and Fig. S2b) and catalysis properties. We then extended our analysis focusing on the *in situ* XAS spectra obtained at Zr and Zn K-edges during activation for this sample. Despite subtle intensity losses, the XANES region of Zr and Zn K-edges of ZrZn-15 catalyst did not change upon the activation procedure (Fig. S12), indicating that oxidation state of both Zn and Zr

was not modified by the activation protocol. In the following, we then describe the results and additional insights obtained from the analysis of the EXAFS region of Zr and Zn K-edges.

3.2.3.1 Zr K-edge

During activation, the phase-uncorrected FT-EXAFS spectra at Zr K-edge in Fig. 10a,c showed a constant intensity decrease, consistent with the increase of the thermal contributions to DW factors. The same t-ZrO_2 structural model described in Section 3.2.1.2 and SI Section 2 (considering Zr-$O_{I/II}$ and Zr-Zr/Zn scattering paths), was applied to each dataset at the ten different temperatures. Complete details on the fit parameters can be found in SI Section 7. Best-fit spectra in Fig. 10b,d and Fig. S13a,b are in good agreement with the experimental data, well describing the Zr-$O_{I/II}$ and Zr-Zr/Zn shells intensity loss and shift. DW factors (Fig. S14a) showed a linear trend rising with temperature while Zr-$O_{I/II}$ radial distances (Fig. S14b) remained constant. Considering the antiphase effect involving Zr-Zr and Zr-Zn scattering paths (Fig. 4c) and the increase of their mean square displacement, directly related to the DW factor, we can justify that their radial distances slightly increase up to reaching the same value, showing that at high temperature we cannot safely distinguish between their relative position. Evaluated Einstein temperatures for Zr-O confirmed the presence of stronger Zr-O_{II} and a weaker Zr-O_{II} bonds, in line with the results discussed in section 3.2.1.2. Consistently with the graphical comparison between experimental and best-fit curves (Fig. 10, Fig. S13), the corresponding R-factor values (Fig. S14c) confirm the reliability of the adopted fitting model.
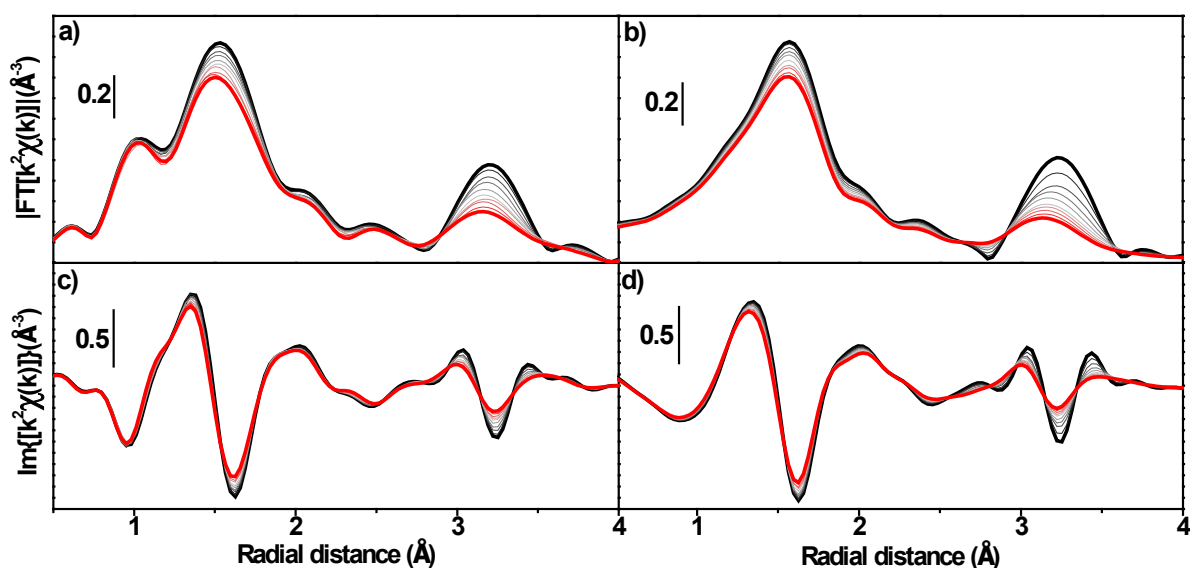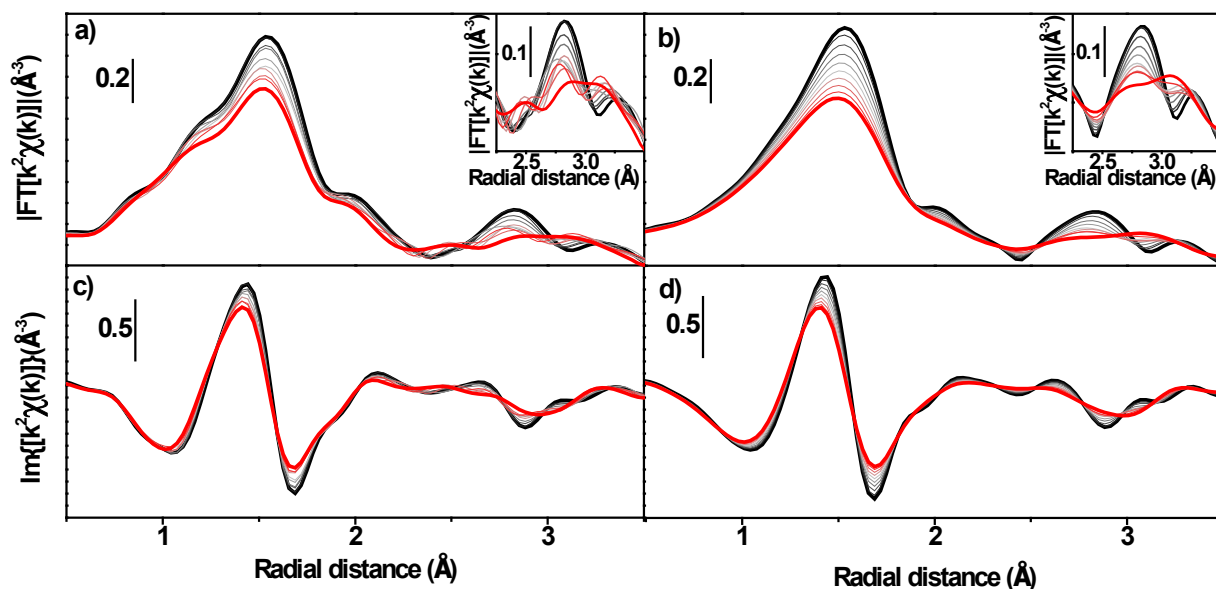
Figure 10. Zr K-edge a, c) experimental and b, d) best fit a, b) magnitude and c, d) imaginary parts of k^2-weighted phase uncorrected FT-EXAFS of ZrZn-15 measured at increasing temperatures (black to red lines) in the RT-400 °C range under H_2 gas flow. Fits are performed in the k-range 2.5-13 Å^{-1} and R-range 1.0-4.0 Å. Details on the fit results are reported in Fig. S13, S14 and Table S6.

3.2.3.2 Zn K-edge

Phase-uncorrected FT-EXAFS at Zn K-edge recorded during thermal activation in Fig. 11a,c showed a constant decrease of the first and second shell intensity related to the increase in DW factors. However, the second shell presents a non-trivial dynamic involving two distinct features. The feature at lower radial distance (≈ 2.8 Å, phase-uncorrected), previously associated to Zn-Zn$_\mathrm{I}$ scattering path, slightly loses intensity. Conversely, the one at higher distance (≈ 3.2 Å), stemming from Zn-Zr and Zn-Zn$_\mathrm{II}$ scattering paths according to the h-ZnO/ZrO$_2$ model described in the previous section, shifts to lower values until it convolutes with the former one at high temperature. As shown in Fig. S17 and Fig. S18, considering the simpler h-ZnO model for fitting the spectra during activation, the second shell temperature evolution would not be described, leading to unphysically high DW factors, larger errors for the radial distances and not reliable R-factors. The presence of Zn-Zr/Zn-Zn$_\mathrm{II}$ scattering paths originated from the h-ZnO/ZrO$_2$ interface must then be considered to describe the temperature dependent evolution of EXAFS signal in the second-shell region. Assuming a constant dimension of

the ZnO cluster during the activation, a single CN for each path was fit for all the dataset while radial distances were left independent for all the paths in the dataset. The fit in Fig. 11c,d and S15 shows a good agreement with the experimental data, especially in reproducing the second-shell dynamics. Here, despite of a little of mismatch in the reproduction of the final intensity, the three contributions of Zn-Zn$_I$, Zn-Zn$_{II}$ and Zn-Zr well described the intensity variation of the two features during heating, up to their convolution at high temperatures. The so-obtained DW factors (Fig. S16a) showed a linear increase with temperature leading, in the case of Zn-Zn$_{I/II}$, to quite high values but still comparable with those obtained at RT. Noteworthy, during heating there is not net radial distance variation in the first coordination shell. Conversely, at high temperature the Zn-Zn$_{II}$/Zr scattering paths in second shell are optimized to almost the same interatomic distance (Fig. S16b), while a distinction is maintained between scattering paths originating from the core of the ZnO cluster (Zn-Zn$_I$) and from its surface (Zr-Zn$_{II}$/Zr). As showed for the Zr K-edge (see section 3.2.1.2), the so introduced Zn-Zr scattering path is in anti-phase with the Zn-Zn$_{II}$, which would have led to a strong correlation between their CN, DW factors and radial distances if the Einstein model would have not been applied. The evaluated Zn-Zn$_I$ CN (5.6 ± 1) (Table S7, S8) is associated to a ZnO cluster radius of 13 ± 3 Å, in good agreement with values obtained from EXAFS analysis of RT data. Reliability of the fit is furthermore confirmed by comparable Einstein temperatures for Zr-Zn (226 ± 26 K) and Zn-Zr (269 ± 24 K) and for Zn-Zn$_I$ (174 ± 25 K) and Zn-Zn$_{II}$ (174 ± 26 K) scattering paths (Table S8). The latter one is matching literature values as well.[52] As showed in Table S7, fit reliability is additionally confirmed as values obtained at 312K/H$_2$ and 300K/He from fits performed with and without the Einstein model, respectively, are entirely comparable.

Figure 11. Zn K-edge a, c) Experimental and b, d) best fit of a, b) magnitude and c, d) imaginary parts of k^2-weighted FT-EXAFS of ZrZn-15 measured at increasing temperatures (black to red lines) in the RT-400 °C range under H_2 gas flow. A magnification of the second-shell region is reported in the insets. Fits are performed in the k-range 2-12 $Å^{-1}$ and R-range 1.0-4.0 Å. Details on the fit results are reported in Fig. S15, S16 and Tables S7, S8.

Noteworthy, the same Zn K-edge second shell dynamic was observed in the FT-EXAFS of ZrZn-30 catalyst reported in Fig. S19. The spectra, collected under the same conditions as for ZrZn-15, showed a thermal DW factor-induced intensity loss for the first and second shell peaks. In the latter, even if a stronger Zn-Zn contribution originating from the segregated ZnO phase is present, it is clear that at high temperature the signal structure follows the same dynamic discussed for ZrZn-15. In the ZrZn-30 case, we could not safely fit the EXAFS spectra, since segregated bulk h-ZnO was observed by PXRD (Fig. 1). However, the quantitative results obtained using ZrZn-15 allowed us to qualitatively interpret the EXAFS spectral evolution for ZrZn-30, the most active catalyst, as originating from the interplay between scattering paths involving the core (Zn-Zn_I) and the surface (Zn-Zn_{II}/Zr) of the ZrO_2-embedded ZnO nanoclusters.

3.2.4 Implications for ZnO clusters and V_o location

By combining ICP analysis and Rietveld refinement of PXRD data, we quantitatively evaluated the amount of Zn loaded in the ZrO_2 structure excluding the bulk ZnO contribution (Table S1). In parallel, by Zr K-edge FT-EXAFS we obtained an indirect information of the Zn doping from second-shell intensity loss (Table 1). Zn coordination number extracted from Zr-Zn second shell fit is associated with its wt.% (Table 1) which, despite of a slight underestimation, falls in line with the values in Table S1. The information found by coupling ICP and PXRD refinement is easily accessible by widespread laboratory methods, but it does not provide chemical insights on the Zn dopant nature. Conversely, the Zn-loading-dependent intensity variations in Zr K-edge second-shell peak shows that EXAFS is sensitive to the guest-host structural/chemical proximity, proving that the Zn atom is not simply segregated or impregnated on zirconia but it is chemically bonded to the oxidic matrix.

The presence of embedded ZnO nanoclusters (Section 3.2.2.2) explains the underestimation in Zn wt.% obtained from Zr K-edge FT-EXAFS fit (Table 1) with respect to what was found by ICP and PXRD Rietveld refinement. In fact, the shell intensity can be influenced only by those Zn atoms which are located on the ZnO cluster surface: the bigger the ZnO cluster, the higher the Zn wt.% underestimation by FT-EXAFS.

As mentioned in Section 3.2.1.2, in our Zr K-edge EXAFS analysis, the variable "*Zn*" used to describe Zr-Zn and Zr-Zr CNs was also simultaneously used for Zr-O CN (i.e., 8 – Zn). CN and DW factors strongly correlate in the EXAFS equation, however, the simultaneous fit of Zr-O and Zr-Zr/Zn with the same variable *Zn* increases the latter reliability. The nature of the catalysis-oriented *in situ* XAS experiment does not allow us to quantify V_O. Nevertheless, as showed in eq. (1), each Zn generates a V_O, leading to an average Zr-O coordination of ZrO_{8-Zn} (where *Zn* is the same variable refined in the EXAFS fit), which would unlikely form a stable t-ZrO_2 phase. We should then consider that the average ZrO_{8-Zn} configuration detected by EXAFS must be realized by combinations of ZrO_8 and ZrO_{8-x} (where x = 1, 2, 3, 4) polyhedra which host the V_O, most likely localized at the periphery of ZrO_2-embedded ZnO clusters. The FWHM of the XANES feature A (Fig. 3), sensitive to Zr local

geometry, shows that a higher concentration of Zn distorts the ZrO_8 double tetrahedra, supporting this hypothesis.

EXAFS spectra at Zr and Zn K-edges of the catalyst are described considering the presence of Zr-Zn and Zn-Zr scattering paths, respectively, for both measurements at RT in He and *in situ* temperature-dependent data collected during activation in H_2. These results confirm that Zn doping occurs with formation of ZnO clusters which surface is chemically bonded to the ZrO_2 matrix. This finally led us to critically observe the variations in Zn K-edge EXAFS spectra of the activated catalysts after exposure to the reaction mixture (CO_2/H_2) under catalysis-relevant conditions. With this respect, some inherent limitations should be considered, mainly related to the following facts: i) the catalysts presented relatively low surface area (46 m^2/g),[20] ii) CO_2/H_2 interactions are limited to the material surface, and iii) XAS is a mainly bulk-sensitive technique. Nonetheless, as shown in Fig. S20, subtle modifications can be noted in the Zn K-edge EXAFS spectra collected before and after the reaction, carried by sending a CO_2/H_2 feed at 300°C/15 bar over activated ZrZn-15 and ZrZn-30. Notably, the scattering features previously assigned to the Zn-Zn_I shell, originating from the ZnO cluster core, is unaltered under reaction conditions. Conversely, the EXAFS feature stemming from the Zn-Zn_{II}/Zr contributions varies after the reaction, suggesting that these scattering paths are those influenced by the coordination of adsorbed reactants and products. These observations, guided by the quantitative analysis of *in situ* EXAFS data presented in Section 3.2.3, consistently suggest that the interface between the ZnO cluster and the ZrO_2 matrix represent the active site towards CO_2 hydrogenation, where molecular events involving CO_2 adsorption/activation, H_2 splitting and CH_3OH production ultimately take place.

4   Conclusions

In the present work, we combined PXRD and XAS to make a step further in the fundamental understanding of Zn-doped ZrO_2 catalysts, active towards CO and CO_2 hydrogenation. The XAS dataset, even if measured in a catalysis-oriented experiment (i.e., on pressed and sieved catalyst

powders hosted in a capillary reactor, at RT or higher temperatures), showed a great potential for clarifying the Zn-doped ZrO_2 atomic-scale structure through parallel analysis of data at Zr and Zn K-edges. While the ZrO_2 $d_{(101)}$ Bragg reflection shift was related to the presence of Zn in the ZrO_2 lattice, the t-ZrO_2 fingerprint peak identified by PXRD, close to the dataset noise, cannot unambiguously identify the ZrO_2 polymorph. However, by coupling analysis of Zr K-edge XANES pre-edge features with EXAFS fitting, we safely confirmed the presence of t-ZrO_2. In addition, Zr K-edge EXAFS fit revealed Zn atoms chemically bonded to Zr, while Zn K-edge EXAFS unveiled the presence of h/c-ZnO clusters. Since previous measurements[20,21] did not show the presence of ZnO nanoparticles on ZrO_2 surface, we assumed the ZnO cluster to be largely embedded in the ZrO_2 matrix, with only a minor fraction exposed at the catalyst surface. Broadening of the size distribution cannot be accessed by EXAFS, whilst details on cluster shape could be only accessed considering a fit extended to the third and fourth coordination shell, which would be unreliable within the available data quality. Yet, under the spherical shape approximation, we were able to estimate the average radius of ZrO_2-embedded ZnO clusters. In particular, a Zn-Zn CN value far from the ideal bulk condition, was refined from Zn K-edge EXAFS analysis of ZrZn-15 (15 wt.% of Zn doping). Relation between EXAFS-determined CN and cluster dimension was calculated by the Greegor and Lytle equation, showing an average radius of 11 ± 5 Å (or 13 ± 3 Å, evaluated from the analysis of *in situ* XAS data), small enough to escape detection by PXRD. Careful analysis of the *in situ* EXAFS data shows the presence of Zn-O-Zr interaction from both Zr and Zn K-edges, supporting the hypothesis that Zn-doped ZrO_2 catalysts consist of ZnO clusters chemically bonded to the ZrO_2 matrix. It is then the ZnO/ZrO_2 interface, where V_O are mostly located, the active phase towards CO_2 hydrogenation. More than increasing the Zn content, improving ZnO/ZrO_2 interface area, is then envisaged as an effective way to maximize the catalyst activity. Taken together, this evidence provides, to the best of our knowledge, the deepest structural picture available so far on Zn-doped ZrO_2 catalysts. While highlighting the richness of information accessible from a wise combination of X-ray methods

probing long-range order and local structure in mixed-metal oxides, the obtained insights pave the way to the rational design of improved catalysts for CO_2 valorisation.

Associated content

Supporting Information

The Supporting Information is available free of charge at https://pubs.acs.org/doi/xxx

K-space EXAFS spectra; additional PXRD results; EXAFS fitting for reference t-ZrO_2; FWHM analysis of first derivative of the Zr K-edge XANES main edge; EXAFS fitting for reference h-ZnO; test Zr K-edge EXAFS fitting of ZrZn-5 using a c-ZrO_2 model; additional details on input structures employed in Zn K-edge EXAFS fitting; additional details on cluster size evaluation; additional details on *in situ* XAS data during activation in H_2 and related EXAFS analysis using the Einstein model; *in situ* XAS data under reaction conditions (CO_2/H_2, 300 °C, 15 bar).

Author information

Corresponding Author

Elisa Borfecchia − Department of Chemistry, NIS Center and INSTM Reference Center, University of Turin, 10125, Turin, Italy; orcid.org/0000-0001-8374-8329; Email: elisa.borfecchia@unito.it

Authors

Davide Salusso − Department of Chemistry and NIS Center, University of Turin, 10125, Turin, Italy; https://orcid.org/0000-0001-7927-4001

Silvia Bordiga − Department of Chemistry, NIS Center and INSTM Reference Center, University of Turin, 10125, Turin, Italy; https://orcid.org/0000-0003-2371-4156

Complete contact information is available at: https://pubs.acs.org/xxx

Notes

The authors declare no competing financial interest

References

(1) Tanabe, K. Surface and Catalytic Properties of ZrO_2. *Mater. Chem. Phys.* **1985**, *13*, 347–364.

(2) Yamaguchi, T. Application of ZrO_2 as a Catalyst and a Catalyst Support. *Catal. Today* **1994**, *20*, 199–217.

(3) Dong, X.; Li, F.; Zhao, N.; Xiao, F.; Wang, J.; Tan, Y. CO_2 Hydrogenation to Methanol over $Cu/ZnO/ZrO_2$ Catalysts Prepared by Precipitation-Reduction Method. *Appl. Catal. B Environ.* **2016**, *191*, 8–17.

(4) Pokrovski, K.; Jung, K. T.; Bell, A. T. Investigation of CO and CO_2 Adsorption on Tetragonal and Monoclinic Zirconia. *Langmuir* **2001**, *17*, 4297–4303.

(5) Rockström, J.; W. Steffen; K. Noone; Å. Persson; F. S. Chapin; E. F. Lambin; T. M. Lenton; M. Scheffer; C. Folke; H. J. Schellnhuber; B. Nykvist; C. A. de Wit; T. Hughes; S. van der Leeuw; H. Rodhe; S. Sörlin; P. K. Snyder; R. Costanza; U. Svedin; M. Falkenmark; L. Karlberg; R. W. Corell; V. J. Fabry; J. Hansen; B. Walker; D. Liverman; K. Richardson; P. Crutzen; J. A. Foley. A Safe Operation Space for Humanity. *Nature* **2009**, *461*, 472–475.

(6) Zhou, W.; Cheng, K.; Kang, J.; Zhou, C.; Subramanian, V.; Zhang, Q.; Wang, Y. New Horizon in C1 Chemistry: Breaking the Selectivity Limitation in Transformation of Syngas and Hydrogenation of CO_2 into Hydrocarbon Chemicals and Fuels. *Chem. Soc. Rev.* **2019**, *48*, 3193–3228.

(7) Cole, M.; Catlow, C. R. A.; Dragun, J. P. EXAFS Studies of Doped-ZrO_2 Systems. *J. Phys. Chem. Solids* **1990**, *51*, 507–513.

(8) Huang, J.; Li, W.; Wang, K.; Huang, J.; Liu, X.; Fu, D.; Li, Q.; Zhan, G. M XO Y-ZrO_2 (M = Zn, Co, Cu) Solid Solutions Derived from Schiff Base-Bridged UiO-66 Composites as High-Performance Catalysts for CO_2 Hydrogenation. *ACS Appl. Mater. Interfaces* **2019**, *11*, 33263–33272.

(9) Chagas, L. H.; Zonetti, P. C.; Matheus, C. R. V.; Rabello, C. R. K.; Alves, O. C.; Appel, L. G. The Role of the Oxygen Vacancies in the Synthesis of 1, 3-Butadiene from Ethanol. *ChemCatChem* **2019**, *11*, 5625–5632.

(10) Silva-Calpa, L. del R.; Zonetti, P. C.; Rodrigues, C. P.; Alves, O. C.; Appel, L. G.; de Avillez, R. R. The $Zn_xZr_{1-x}O_{2-y}$ Solid Solution on m-ZrO_2: Creating O Vacancies and Improving the m-ZrO_2 Redox Properties. *J. Mol. Catal. A Chem.* **2016**, *425*, 166–173.

(11) Wang, C.; Garbarino, G.; Allard, L. F.; Wilson, F.; Busca, G.; Flytzani-Stephanopoulos, M. Low-Temperature Dehydrogenation of Ethanol on Atomically Dispersed Gold Supported on ZnZrOx. *ACS Catal.* **2016**, *6*, 210–218.

(12) Han, S.; Zhao, D.; Otroshchenko, T.; Lund, H.; Bentrup, U.; Kondratenko, V. A.; Rockstroh, N.; Bartling, S.; Doronkin, D. E.; Grunwaldt, J. D.; Rodemerck, U.; Linke, D.; Gao, M.; Jiang, G.; Kondratenko, E. V. Elucidating the Nature of Active Sites and Fundamentals for Their Creation in Zn-Containing ZrO_2-Based Catalysts for Nonoxidative Propane Dehydrogenation. *ACS Catal.* **2020**, *10*, 8933–8949.

(13) Zhou, S.; Li, S. Insights into the High Activity and Methanol Selectivity of the Zn/ZrO_2 Solid Solution Catalyst for CO_2 Hydrogenation. *J. Phys. Chem. C* **2020**, *124*, 27467–27478.

(14) Aghabeygi, S.; Khademi-Shamami, M. ZnO/ZrO_2 Nanocomposite: Sonosynthesis, Characterization and Its Application for Wastewater Treatment. *Ultrason. Sonochem.* **2018**, *41*, 458–465.

(15) Wu, X.; Tan, M.; Tian, S.; Song, F.; Ma, Q.; He, Y.; Yang, G.; Tsubaki, N.; Tan, Y. Designing ZrO_2-Based Catalysts for the Direct Synthesis of Isobutene from Syngas: The Studies on Zn Promoter Role. *Fuel* **2019**, *243*, 34–40.

(16) Liu, X.; Zhou, W.; Yang, Y.; Cheng, K.; Kang, J.; Zhang, L.; Zhang, G.; Min, X.; Zhang, Q.; Wang, Y. Design of Efficient Bifunctional Catalysts for Direct Conversion of Syngas into Lower Olefins: Via Methanol/Dimethyl Ether Intermediates. *Chem. Sci.* **2018**, *9*, 4708–4718.

(17) Liu, Y.; Xia, C.; Wang, Q.; Zhang, L.; Huang, A.; Ke, M.; Song, Z. Direct Dehydrogenation of Isobutane to Isobutene over Zn-Doped ZrO_2 Metal Oxide Heterogeneous Catalysts. *Catal. Sci. Technol.* **2018**, *8*, 4916–4924.

(18) Cheng, K.; Zhou, W.; Kang, J.; He, S.; Shi, S.; Zhang, Q.; Pan, Y.; Wen, W.; Wang, Y. Bifunctional Catalysts for One-Step Conversion of Syngas into Aromatics with Excellent Selectivity and Stability. *Chem* **2017**, *3*, 334–347.

(19) Shannon, B. Y. R. D.; H, M.; Baur, N. H.; Gibbs, O. H.; Eu, M.; Cu, V. Revised Effective Ionic Radii and Systematic Studies of Interatomie Distances in Halides and Chaleogenides.

Acta Crystallogr. Sect. A Found. Crystallogr. **1976**, *32*, 751–767.

(20) Ticali, P.; Salusso, D.; Ahmad, R.; Ahoba-sam, C.; Ramirez, A.; Shterk, G.; Lomachenko, K. A.; Borfecchia, E.; Morandi, S.; Cavallo, L.; Gascon, J.; Bordiga, S.; Olsbye, U. CO_2 Hydrogenation to Methanol and Hydrocarbons over Bifunctional Zn-Doped ZrO_2/ Zeolite Catalysts. *Catal. Sci. Technol.* **2021**, *11*, 1249–1268.

(21) Wang, G.; Zeng, L.; Cao, J.; Liu, F.; Lin, Q.; Yi, Y.; Pan, H. Highly Selective Conversion of CO_2 to Hydrocarbons over Composite Catalysts of ZnO-ZrO_2 and SAPO-34. *Microporous Mesoporous Mater.* **2019**, *284*, 133–140.

(22) Li, Z.; Qu, Y.; Wang, J.; Liu, H.; Li, M.; Miao, S.; Li, C. Highly Selective Conversion of Carbon Dioxide to Aromatics over Tandem Catalysts. *Joule* **2019**, *3*, 570–583.

(23) Zhang, T. ZnO-ZrO_2 Solid Solution Catalyst for Highly Selective Hydrogenation of CO_2 to Methanol. *Cuihua Xuebao/Chinese J. Catal.* **2017**, *38*, 1781–1783.

(24) Murthy, P. S.; Liang, W.; Jiang, Y.; Huang, J. Cu-Based Nanocatalysts for CO_2 Hydrogenation to Methanol. *Energy Fuels* **2021**, *35*, 8558–8584.

(25) Greegor, R. B.; Lytle, F. W. Morphology of Supported Metal Clusters : Determination by EXAFS and Chemisorption. *J. Catal.* **1980**, *63*, 476–486.

(26) Rodríguez-Carvajal, J. Recent Developments of the Program Fullprof. *Newsl. Comm. Powder Diffr. IUCr* **2001**, *26*, 12–19.

(27) Thompson, P.; Cox, D. E.; Hastings, J. B. Rietveld Refinement of Debye-Scherrer Synchrotron X-Ray Data from Al_2O_3. *J. Appl. Crystallogr.* **1987**, *20*, 79–83.

(28) La Fontaine, C.; Belin, S.; Barthe, L.; Roudenko, O.; Briois, V. ROCK: A Beamline Tailored for Catalysis and Energy-Related Materials from ms Time Resolution to mm Spatial Resolution. *Synchrotron Radiat. News* **2020**, *33*, 20–25.

(29) Ravel, B.; Newville, M. ATHENA , ARTEMIS , HEPHAESTUS : Data Analysis for X-Ray Absorption Spectroscopy Using IFEFFIT. *J. Synchrotron Radiat.* **2005**, *12*, 537–541.

(30) Momma, K.; Izumi, F. VESTA 3 for Three-Dimensional Visualization of Crystal, Volumetric and Morphology Data. *J. Appl. Crystallogr.* **2011**, *44*, 1272–1276.

(31) Rehr, J. J.; Albers, R. C. Theoretical Approaches to X-Ray Absorption Fine Structure. *Rev. Mod. Phys.* **2000**, *72*, 621–654.

(32) Zabinsky, S. I.; Rehr, J. J.; Ankudinov, A.; Albers, R. C.; Eller, M. J. Multiple-Scattering Calculations of x-Ray-Absorption Spectra. *Phys. Rev. B* **1995**, *52*, 2995–3009.

(33) Teufer, G. The Crystal Structure of Tetragonal ZrO$_2$. *Acta Crystallogr.* **1962**, *15*, 1187.

(34) Kröger, F. A.; Vink, H. J. Relations between the Concentrations of Imperfections in Crystalline Solids. *Solid State Phys. - Adv. Res. Appl.* **1956**, *3*, 307–435.

(35) Abrahams, S. C.; Bernstein, J. L. Remeasurement of the Structure of Hexagonal ZnO. *Acta Crystallogr. Sect. B Struct. Crystallogr. Cryst. Chem.* **1969**, *25*, 1233–1236.

(36) Bragg, W. L. ; Darbyshire, J. A. The Structure of Thin Films of Certain Metallic Oxides. *Trans. Faraday Soc.* **1932**, *32*, 522–529.

(37) Sevillano, E.; Meuth, H.; Rehr, J. J. Extended X-Ray Absorption Fine Structure Debye-Waller Factors. I. Monatomic Crystals. *Phys. Rev. B* **1979**, *20*, 4908–4911.

(38) Braglia, L.; Borfecchia, E.; Martini, A.; Bugaev, A. L.; Soldatov, A. V.; Øien-ØDegaard, S.; Lønstad-Bleken, B. T.; Olsbye, U.; Lillerud, K. P.; Lomachenko, K. A.; Agostini, G.; Manzoli, M.; Lamberti, C. The Duality of UiO-67-Pt MOFs: Connecting Treatment Conditions and Encapsulated Pt Species by: Operando XAS. *Phys. Chem. Chem. Phys.* **2017**, *19*, 27489–27507.

(39) Øien, S.; Agostini, G.; Svelle, S.; Borfecchia, E.; Lomachenko, K. A.; Mino, L.; Gallo, E.;

Bordiga, S.; Olsbye, U.; Lillerud, K. P.; Lamberti, C. Probing Reactive Platinum Sites in Uio-67 Zirconium Metal-Organic Frameworks. *Chem. Mater.* **2015**, *27*, 1042–1056.

(40) Fornasini, P.; Grisenti, R. On EXAFS Debye-Waller Factor and Recent Advances. *J. Synchrotron Radiat.* **2015**, *22*, 1242–1257.

(41) Martin, U.; Boysen, H.; Frey, F. Neutron Powder Investigation of Tetragonal and Cubic Stabilized Zirconia, TZP and CSZ, at Temperatures up to 1400 K. *Acta Crystallogr. Sect. B* **1993**, *49*, 403–413.

(42) Frandon, J.; Brousseau, B.; Pradal, F. Electronic Excitations in Some Transition Metals and Their Oxides. *Phys. Status Solidi* **1980**, *379*, 379–385.

(43) Li, P.; Chen, I. W.; Penner-Hahn, J. E. X-Ray-Absorption Studies of Zirconia Polymorphs. I. Characteristic Local Structures. *Phys. Rev. B* **1993**, *48*, 10063–10073.

(44) Li, P.; Chen, I. W.; Penner-Hahn, J. E. X-Ray-Absorption Studies of Zirconia Polymorphs. III. Static Distortion and Thermal Distortion. *Phys. Rev. B* **1993**, *48*, 10082–10089.

(45) Gilbert, B.; Frazer, B. H.; Zhang, H.; Huang, F.; Banfield, J. F.; Haskel, D.; Lang, J. C.; Srajer, G.; De Stasio, G. X-Ray Absorption Spectroscopy of the Cubic and Hexagonal Polytypes of Zinc Sulfide. *Phys. Rev. B - Condens. Matter Mater. Phys.* **2002**, *66*, 1–6.

(46) Wilmer, H.; Kurtz, M.; Klementiev, K. V.; Tkachenko, O. P.; Grünert, W.; Hinrichsen, O.; Birkner, A.; Rabe, S.; Merz, K.; Driess, M.; Wöll, C.; Muhler, M. Methanol Synthesis over ZnO: A Structure-Sensitive Reaction? *Phys. Chem. Chem. Phys.* **2003**, *5*, 4736–4742.

(47) Wang, J.; Li, G.; Li, Z.; Tang, C.; Feng, Z.; An, H.; Liu, H.; Liu, T.; Li, C. A Highly Selective and Stable ZnO-ZrO$_2$ Solid Solution Catalyst for CO$_2$ Hydrogenation to Methanol. *Sci. Adv.* **2017**, *3*, 1–11.

(48) Agostini, G.; Piovano, A.; Bertinetti, L.; Pellegrini, R.; Leofanti, G.; Groppo, E.; Lamberti,

C. Effect of Different Face Centered Cubic Nanoparticle Distributions on Particle Size and Surface Area Determination: A Theoretical Study. *J. Phys. Chem. C* **2014**, *118*, 4085–4094.

(49)   Frenkel, A. I.; Yevick, A.; Cooper, C.; Vasic, R. Modeling the Structure and Composition of Nanoparticles by Extended X-Ray Absorption Fine-Structure Spectroscopy. *Annu. Rev. Anal. Chem.* **2011**, *4*, 23–39.

(50)   Frenkel, A. I. Applications of Extended X-Ray Absorption Fine-Structure Spectroscopy to Studies of Bimetallic Nanoparticle Catalysts. *Chem. Soc. Rev.* **2012**, *41*, 8163–8178.

(51)   Kuzmin, A.; Chaboy, J. EXAFS and XANES Analysis of Oxides at the Nanoscale. *IUCrJ* **2014**, *1*, 571–589.

(52)   Tchuigoua, B. H.; Sendja, B. T.; Mane, J. M.; Aquilanti, G.; Plaisier, J. R. EXAFS Study of the Temperature Dependence of the Debye-Waller Factor in ZnSe Zincblende Compound. *Phys. Scr.* **2020**, *95*, 045704.

TOC Graphic